2015227_Table S1

SI.1: Sample and Geologic Background

This study used a sample of spherulite-bearing obsidian collected from Pitchstone Plateau lava flow from Yellowstone caldera (Fig. S1). The upper pumiceous carapace of the lava has been stripped away by Pinedale glaciations, but both the preservation of pressure ridges and the low dissolved water content (0.1 wt.%) in the glass indicate the sample was collected from the upper portion the flow (Christiansen 2001). Pitchstone Plateau is the largest lava flow (70 km^3) from the Central Plateau Member Rhyolites, which consist of ~30 high silica rhyolitic obsidian lava flows and domes with flow thicknesses that range from 17 to 200 m and have eruptive volumes ranging from 0.001 to 70 km^3. The lavas were erupted during an era of predominantly effusive activity from 79 to 166 ka in Yellowstone caldera, with Pitchstone Plateau being one of the youngest (79±10 ka) (Christiansen et al. 2007). The Central Plateau Member rhyolites are compositionally similar, and are composed of high silica rhyolite glass with phenocrysts of quartz, sanidine, clinopyroxene, and magnetite (Christiansen 2001).

SI.2: Trace element and water measurements

Trace-element concentrations were measured by LA-ICP-MS at the University of Texas at Austin in four separate analytical sessions, using a New Wave Research UP 193-FX fast excimer (193nm wavelength, 4-6 ns pulse width) laser system coupled to an Agilent 7500ce ICP-MS. The laser system is equipped with a large format, two-volume laser cell, for direct sampling of the ablation plume with fast (< 1s) washout times to minimize spatial carryover. Laser ablation parameters optimized from spherulite test ablations were 5 μm s^{-1} line traverses using a 10x100 μm rectangular slit aperture with long-axis normal to the scan direction, 70% power, 10 Hz repetition rate, and He cell flows of 200-300 mL min^{-1}. Laser energy densities (fluences)

obtained for all sessions averaged 1106 J cm^{-2} with < 3% variation. The ICP-MS operated at an RF power of 1600 W and an average Ar carrier flow of 1.29 L min^{-1}. Oxide production rates as monitored by ThO/Th for NIST 612 were ≤ 0.21%. The quadrupole time-resolved method involved measurement of 14 masses (^{7}Li, ^{11}B, ^{23}Na, ^{25}Mg, ^{29}Si, ^{39}K, ^{45}Sc, ^{55}Mn, ^{85}Rb, ^{88}Sr, ^{133}Cs, ^{137}Ba, and ^{208}Pb) using integration times between 5 and 100 ms. The analytical sampling period of 0.75 s, equivalent to a reading every 3.7 μm, corresponds to 95.7% measurement time. Time-resolved intensities were converted to concentration (ppm) equivalents using Iolite software (Univ. Melbourne), with ^{29}Si as the internal standard. Baselines were determined from 60 s glass blank intervals measured while the laser was off and all masses were scanned by the quadrupole. NIST 612 was used as the primary reference standard for all analytes. Recoveries (relative 1σ deviations versus GeoREM preferred values) among analytes for a secondary standard (NIST 610), run as an unknown against the primary standard were typically better than 2%. Based on those observations we conservatively assign 5% as relative uncertainties. Laser traverses on sample wafers were oriented along radial projections from spherulite centers, typically beginning within the spherulite and continuing across the spherulite-matrix boundary far into (>1000 μm) the host matrix glass. Element concentrations were calculated assuming a concentration of 77 wt.% SiO_2 in the matrix glass and spherulite. Such a value is equivalent to the overall SiO_2 concentration within spherulites based on the relative proportions of quartz (100 wt.% SiO_2) and alkali feldspar (66 wt.% SiO_2) observed in the spherulites. An SiO_2 concentration of 66 wt.% SiO_2 was used to calculate element concentrations in the porous spherulite rims, which are comprised of alkali feldspar.

The LA-ICP-MS data were collected using a continuous scan, which averages or smooths the data averaged. Although the data is indeed smoothed, we do not deconvolute the data.

Convolution becomes problematic when the scale of the diffusion profile is greater than the scale of the slit used during data collection. The resolution of the trace element data depends on the speed of the transect and the width of the slit. By using a 10 μm slit that traversed the sample at 5 μm s^{-1}, we have spatial resolution of less than 5 μm (3.7 μm). Further, the washout time for the laser cell is <1 s. Thus scanning at 5 μm s^{-1}, with a 10 μm wide slit, it is unlikely that the line scans smooth or miss concentration gradients any wider than 5-10 μm. The Rb diffusion profiles we measure extend hundreds of μm from the spherulite-glass boundary. Thus, our resolution is sufficiently high to resolve the profile with great certainty without deconvolving the trace element data.

Dissolved water contents of the host obsidian were measured by Fourier-Transform Infrared (FTIR) spectroscopy along linear traverses near the LA-ICP-MS laser tracks. The majority of the FTIR analyses were performed by synchrotron-source light at the Advanced Light Source at Lawrence Berkeley National Laboratory using a Nicolet 760 FTIR spectrometer and a Spectra-Tech Nic-Plan IR microscope. Spectra were collected in <5 μm areas every 10 to 20 μm along the linear transects in mid-IR range using a KBr beamsplitter and consist of 60 scans collected at a resolution of 8 cm^{-1}. A set of FTIR analyses were also collected using a Thermo Electron Nicolet 6700 spectrometer and Continuμm IR microscope at the University of Texas at Austin. For those, spectra were collected in mid-IR range using a KBr beamsplitter and a globar source. Spectra consisted of 60 scans collected at a resolution of 4 cm^{-1}. Analytical spots 10 μm wide by 40 μm long were collected every 10 μm along linear transects. Although the spatial resolution of the spectra collected using the synchrotron-source is superior, the spectra collected using either FTIR system are generally indistinguishable.

Total H_2O contents for synchrotron and FTIR measurements were estimated using the absorbance at ~3500 cm^{-1} and a modified Beer-Lambert law. Background of the absorbance at ~3500 cm^{-1} was assumed to be linear. The molar absorptivity of H_2O at ~3500 cm^{-1} was assumed to be 100 L mol^{-1} cm^{-1}, an appropriate absorptivity for low water contents when the water speciation is predominantly hydroxyl (Newman et al. 1986). Glass density was assumed to be 2350 g L^{-1}, and was not adjusted for water content. The thickness of the sample at every analytical spot along each linear transect was measured optically using a petrographic microscope by focusing on the top and bottom of the sample and measuring the distance traveled by the microscope stage with a Heidenhain focus drive linear encoder.

To constrain the behavior of water speciation in the samples, we measured short transects in the near-IR range using a CaF_2 beamsplitter and white light. Absorbances of molecular water (H_2O_m) and hydroxyl (OH^-) were measured at ~5230 cm^{-1} and at ~4500 cm^{-1}, respectively. Background for the absorbances at ~5230 cm^{-1}, and ~4500 cm^{-1} were treated as linear, and thickness was measured as described above. Concentrations of H_2O_m and OH^- were calculated using the model of Zhang et al. (1997).

H_2O concentrations form Type 2 profiles. H_2O concentrations in the glass far from the spherulites are ~0.10 wt.%. Approaching the spherulite rim, H_2O concentrations increase from background values to concentrations as great as 0.37 wt.%. Concentrations statistically above background extend 340 to 1500 μm from the spherulite rim. H_2O abruptly increases in concentration within 50-100 μm of the rim in many samples. Watkins et al. (2009) attributed similar steep enrichments at spherulite rims to hydration processes unrelated to spherulite growth. To test for late-stage hydration, we analyzed H_2O speciation along traverses in the enrichment profiles and background matrix far from spherulites. In the background and gradually

sloping concentration profiles, the majority of the H_2O occurs as hydroxyl (OH^-), as would be expected for H_2O speciation at high temperatures (Newman et al., 1986) (Fig. S2). In the steep portions, near the spherulite rims, the majority of the H_2O occurs as molecular water (H_2O_{mol}). Analytical traverses that cross cracks in the glass are also marked by steep concentration gradients that range up to 0.40 wt.% H_2O, and are largely comprised of H_2O_{mol}. In addition, the steep H_2O enrichments extend ~50 um from both spherulite rims and cracks in the matrix glass. Together, the speciation and enrichment distances suggest that late stage hydration created the sharp H_2O increases, and are thus not included in our investigation. If the abrupt increase is not included, H_2O concentrations at the rim range from 0.12 to 0.18 wt.%.

To investigate the response, or lack thereof, of other elements to late stage hydration, we present LA-ICP-MS analytical traverses that crossed a crack far from the spherulite-matrix boundary (Fig. S3). We found that no elements display enrichments or depletions near the crack in the matrix glass, thus we conclude element concentrations were not modified during late state hydration in concert with water. Further, if the enrichments in Rb and H_2O at spherulite-matrix boundaries were purely an artifact of secondary hydration, then there should be no cause for the observed systematic variations in those gradients with spherulite size.

Overall, profiles were measured across 19 spherulites with radii that range from 500 to 4400 μm. All of the measured Rb and H_2O profiles were used, none were discarded as spurious. Three of the spherulites were analyzed multiple times to test reproducibility. In those tests we found repeat analyses yield uncertainties of 2% to 30%.

SI.3: Differential scanning calorimetry

The thermal history of the obsidian sample was estimated by differential scanning calorimetry (DSC) using a Netzsch ® DSC 404C Pegasus differential scanning calorimeter at the Ludwig-Maximilian University of Munich, Germany, under a constant flow of Argon 5.0 to avoid oxidation of the samples during the heat flux measurements (μV). Pristine, crystal-free obsidian chips were cleaned and stored in a dessicator for 24 hours. A 28 mg sample of the glassy material was loaded into a circular Pt crucible and then closed with a Pt lid. The sample was reheated at 10 °C min^{-1} until it surpassed its glass transition temperature becoming a supercooled liquid, and was further heated for at least ~50 °C above the glass transition to assure complete enthalpic relaxation of the glass. The sample was then cooled and reheated repeatedly at matching rates (25, 20, 15 and 10 °C min^{-1}) to produce 4 calibration curves. A baseline was subtracted from the obtained heat flux traces and the heat capacity (C_p) of the sample was calculated using the heat capacity of a single sapphire crystal.

The glass transition represents a temperature interval where the structure of the glass relaxes and locally equilibrates to the ambient temperature and pressure, i.e., to the liquid state. Peak glass transition temperatures (T_g peak)(influenced both by the previous cooling rate and actual heating rate) correspond to crests when plotting heat capacity against temperature. Each calibrated C_p curve was modeled following the phenomenological Tool-Narayanaswamy-Moynihan (TNM) approach (Tool, 1946; Narayanaswamy, 1971; Moynihan, et al. 1976), and using the rewritten equations from DeBolt et al. (1976) and the procedure outlined in Wilding et al. (1995). Activation enthalpy ΔH and pre-exponential factor A were calculated respectively from the slope and intercept of the fitted line formed by plotting –ln(cooling rate) against $1/T_g$ peak. Parameters x and β were estimated for each calibration curve and averaged. Lastly, the natural cooling rate of the obsidian was estimated with the TNM approach by modeling the C_p

curve obtained with the first reheating of the sample, and using the 4 previously determined parameters. The resulting cooling rate corresponded to the curve fit with the least sum of squared residuals.

For a heating rate of 25 K min^{-1} during the first heating treatment, the peak glass transition temperature is 736±1 °C, and for a cooling and heating rate of 10 K min^{-1}, 733 ±1 °C (Fig. S4). Those temperatures are significantly higher than estimates of 600-670° C calculated or measured for a rhyolitic melt (Hess and Dingwell, 1996; Dingwell, 1998; Giordano et al., 2008). The TNM modeling approach produced a cooling rate estimate for the Yell-24 obsidian sample of $10^{-5.3}$ °C s^{-1} with an uncertainty of +0.2 log units and -0.5 log unit, equivalent to 0.47±0.30 °C day^{-1}. The high overshoot is characteristic of slowly-cooled glasses. The fit of the model curve to the natural C_p curve is very good with a sum of squared residuals of 1.05. The 4 parameter values used to model the natural C_p curve are for ΔH, 2.91e-05 J mol^{-1}, A, 6.4e-14 s, x, 0.91 and β, 0.71. The calibration C_p curves were relatively noisy, which rendered the determination of peak and supercooled liquid temperatures difficult, but we were consistent in selecting the temperatures and are confident that they are realistic.

SI.4: Numerical Model

To model spherulite growth we assume spherulites grow by crystallization of rhyolitic melt or glass in response to undercooling (e.g. Keith and Padden, 1963; Lofgren, 1971a; Lofgren, 1971b; Fenn, 1977; Swanson, 1977). The mineralogy of the natural spherulites does not change significantly from core to rim, thus we treat the spherulite aggregate as a homogenous, spherical phase. With each increment of growth spherulites expel incompatible elements to the external melt or glass (Keith and Padden, 1964; Lofgren, 1971b; Smith et al., 2001). We employ

empirical bulk fractionation factors in the model that are based on the analyzed element concentration differences between the spherulite interior and surrounding matrix (e.g., 50% and 70% for Rb and H_2O, respectively). Our empirical approach obviates the need for theoretical or experimental estimates for partitioning between crystalline phases and glass. We consider such an approach a strength to the model because of complexities associated with possible disequilibrium kinetics and crystallization of quartz variety (alpha, beta, or cristobalite) and feldspar solid solutions. Comparisons between empirical element partitioning during spherulite growth and magmatic, equilibrium growth would be interesting, but is beyond the scope of this project. Incompatible elements are concentrated in the surrounding matrix, and diffuse away from the spherulite-matrix boundary with time. Thus, the concentration of incompatible elements surrounding spherulites is controlled by spherulite growth rate and elemental diffusivity. To simulate this advection-diffusion process, we use finite-difference numerical modeling to solve the radial diffusion equation:

$$\left(\frac{\partial C}{\partial t}\right)_i = \frac{1}{r^2} * \frac{\partial}{\partial r} * (D_i * r^2 * \left(\frac{\partial C}{\partial r}\right)_i) \quad (1)$$

where $\left(\frac{\partial C}{\partial t}\right)_i$ is the concentration of the incompatible constituent *i* at time *t*, $\left(\frac{\partial C}{\partial r}\right)_i$ is the concentration of *i* at a radial distance from the spherulite boundary *r*, and D_i is diffusivity of *i*. D_i varies with temperature following

$$D_i = D_{O,i} exp\left(\frac{-E_{A,i}}{RT}\right) \quad (2)$$

where $D_{o,i}$ is a constant, $E_{A,i}$ is the activation energy, R is the gas constant, and T is temperature (°C). Values for $D_{o,i}$ and $E_{A,i}$ are from Ni and Zhang (2008) and Zhang et al. (2010). Advection is modeled by simulating the motion of the spherulite-matrix boundary with time, and is controlled by the radial growth rate of the spherulite. Following Gardner et al. (2012), we assume radial-controlled spherulite growth, where each increment of growth adds mass as a proportion of its radius and expels incompatible elements. Our model can simulate a constant radial growth, or radial rates that linearly or exponentially with cooling, as follows

Constant $$\left(\frac{dR}{dt}\right) = \left(\frac{dR}{dt}\right)_O \quad (3)$$

Linearly decreasing $$\left(\frac{dR}{dt}\right) = \left(\frac{dR}{dt}\right)_O - \left(\frac{dR}{dt}\right)_O * \frac{(T_f - T_o)}{(T - T_o)} \quad (4)$$

Exponentially decreasing $$\left(\frac{dR}{dt}\right) = \left(\frac{dR}{dt}\right)_O * exp(-a * (T - T_o)) \quad (5)$$

where $\left(\frac{dR}{dt}\right)$ is the radial growth rate at a specific timestep, $\left(\frac{dR}{dt}\right)_O$ is the initial radial growth rate, T is the temperature model at a specific time (°C), T_o is the initial temperature in the model (°C), T_f is the final temperature in the model (°C), and a is an exponential fit parameter.

Temperature exerts a fundamental control on constituent diffusivity and the growth laws in our model. During model simulations temperature decreases with time (t) from the eruption temperature (T_O) to a final temperature where spherulite growth ceases (T_f) following

$$T = T_O \exp(-(bt)^n) \quad (6)$$

where b and n are fit parameters.

The numerical model is governed by two boundary conditions. First, mass conservation during diffusion and incremental growth is maintained through a Neumann condition (e.g., flux), which ensures that the diffusive fluxes on either side of each cell are the same (LeVeque, 2002). Second, the bulk element concentration is set to a fixed value far into the surrounding matrix.

SI.5: Model Uncertainty

Overview

The purpose of this section is to discuss further the confidence intervals that we have assigned to model parameters. In Fig. 2 we compared model curves to measured data to bracket the spherulite growth rate and cooling rate of the host lava. The advantage of Fig. 2a and 2b is that data from any spherulite can be plotted against the model curves. By comparing the model curves in Fig. 2a and 2b with the Rb and H_2O data, we calculate the spherulite growth rate and lava cooling rate indicated by each data point. The average and standard deviation of those values represent the growth and cooling rate estimates that are provided in the text (Lines 160-170). The disadvantage of that technique is that the model curves are representative of only one nucleation temperature, whereas spherulites of different size likely nucleated at different temperatures. Consequently, our estimates for spherulite growth and lava cooling are conservative values because some of the variation must be caused by variation in the nucleation temperature. Fig. 2A, for example, shows that a range in nucleation temperature of ±75 °C can encompass the entire data set for a single, fixed cooling rate.

Below we present an alternative approach for modeling the data from three spherulites of different size and show that spherulites can indeed be used to infer an accurate and unique value for the growth rate and cooling rate, independent of DSC measurements.

Monte Carlo search of parameter space

To establish the range of cooling rates and growth rates that can adequately fit the data, we run the model over a broad range in parameter space and perform a search for the model profiles that adequately fit the measured data. We treat $n = 1.5$, $a = 0.025$ and $K_D = 0.75$ as constants while varying $(dR/dt)_{initial}$ (defined as the temperature-dependent growth rate extrapolated to 750 °C) and the cooling rate through b. The value for n comes from a conductive cooling model (cf. Manley et al., 1992 and Gardner et al., 2012). The value for c is used to define an exponentially decreasing radial growth law. The assumption of a $K_D = 0.75$ is to minimize the number of free parameters. In the future it may be necessary to relax this assumption because the bulk K_D will vary with the proportion of quartz and sanidine as well as the temperature history of each spherulite.

The algorithm we use is:

- Fix values for $(dR/dt)_{initial}$ and b.
- Calculate by iteration the ``correct" nucleation temperature to fit the radius of the spherulite.
- Run the spherulite growth model to produce a model curve for $(dR/dt)_{initial}$, b, and T_{nuc}.
- Record both the model enrichment at the spherulite boundary and model concentration at the propagation distance. This information is used for comparison to the measured profiles.
- Fix new values for $(dR/dt)_{initial}$ and b and repeat for the entire specified grid of parameter space.

The range and spacing of parameters we explore is $(dR/dt)_{initial}$ = 10 to 140 μm hr^{-1}, equivalent to $(dR/dt)_{at\ 600\ °C}$ of 0.3 to 3.3 μm hr^{-1}, and b ~ 2 to 200 x 10^{-9} °C s^{-1}.

Model applied to one spherulite

Fig. S6a shows the best-fit profile for a medium-sized spherulite Y24-13 (radius = 2050 μm). The parameters used to achieve this best-fit are $(dR/dt)_{initial}$ = 50 μm hr^{-1} and b = 1.82 x 10^{-9} °C s^{-1}. It should be emphasized that these values are non-unique owing to the trade-off between growth rate and cooling rate. There are many other choices of parameters that can achieve equally good fits to the data. To demonstrate this and to assess the range of permissible parameter values, we define an acceptable goodness-of-fit as any model curve that passes through the gray boxes located at the spherulite boundary and *e*-fold distance in Fig. S6a. Note that unlike the approach used in Fig. 2 of the main text, we are using the enrichment and *e*-fold distance separately (and not the ratio of the two) as a unique description of the shape of an individual diffusion profile. The histograms in Fig. S6b-d show the number of model runs for which an acceptable fit was achieved as a function of each of the input parameters. From analysis of a single spherulite, one might conclude that the spherulite nucleated between 500° C to 700 °C, had an initial growth rate of 35 - 65 μm hr^{-1}, and experienced cooling rates between 10^{-5} to 10^{-6} °C s^{-1} (corresponding to b = 19 x 10^{-9} °C $s^{-1}$and b = 1.9 x 10^{-9} °C s^{-1}, respectively), though a much higher cooling rate of $10^{-4.2}$ °C s^{-1} (b ~ 140 x 10^{-9} °C s^{-1}) is also possible. Clearly, analysis of a single spherulite does not provide good constraints on the environmental conditions of spherulite growth.

Model applied to three spherulites

The constraints on spherulite growth parameters improve substantially when we apply the model to three spherulites simultaneously. The algorithm is the same as above, except that each spherulite has a unique nucleation temperature to yield the correct radius. In all model runs, all three spherulites experience the same growth rate at a given temperature and the same cooling rate of the host lava. Fig. S7a-c show that a reasonably good fit can be achieved on all three spherulites despite the many simplifying assumptions that are built into the model. The parameters used to achieve this best-fit are $(dR/dt)_{initial}$ = 55 μm hr^{-1} and b = 9.0 x 10^{-9} °C s^{-1}. As in Fig. S6a, the gray boxes represent the range of permissible model curves and the histograms show the range of parameter values and nucleation temperatures that yield acceptable fits to the data. For the same exact parameter grid as used in the analysis of one spherulite, there are far fewer acceptable model runs that can fit all three spherulites simultaneously.

From analysis of these three spherulites of different sizes, one could deduce that the spherulites nucleated between 490° C and 630 °C, had an initial growth rate of 55 - 60 μm hr^{-1} ($(dR/dt)_{Tnuc}$ = 0.1 to 3.0 μm hr^{-1}) and experienced a cooling rate between 10^{-5} to 10^{-6} °C s^{-1} (corresponding to b = 19 x 10^{-9} °C s^{-1} and b = 1.9 x 10^{-9} °C s^{-1}, respectively), with higher cooling rates being excluded. This range of cooling rates is independent of, yet in excellent agreement with, the value measured by DSC of $10^{-5.3}$ °C s^{-1} (b = 10 x 10^{-9} °C s^{-1}). Parameter values within this quoted range can fit the Rb data from any of the other spherulites and therefore represents another of assigning a conservative estimate for the uncertainty in model parameters that is in agreement with the values we deduced by analysis of Fig. 2. We reiterate, however, that the greatest source of uncertainty in the model epistemic in nature, i.e., the question of whether certain assumptions (e.g., conductive cooling, exponentially decreasing radial growth law, constant K_D) are valid. Although the T_{nuc} values overlap, there is a general agreement that large

spherulites nucleate at higher *T* than small spherulites. This is dictated by setting $(dR/dt)_{initial}$ for all spherulites as the same, but still we were able to get convergence for a with what appear to be a realistic order of T_{nuc} for the three different spherulites. It also supports the conclusion in a general sense of Fig. 2 of the main paper.

FIGURE CAPTIONS

SI Figure 1. Simplified geologic map of the southern portion of the Yellowstone volcanic field surrounding Pitchstone Plateau (modified from Christiansen 2001). The circle marks the sample location (Yell-24). Central Plateau Member Rhyolites are shown in light pink. Dark pink lines on individual flows demark lines of equal flow. The proposed vent location is shown by a small dark pink star. The margin of Yellowstone caldera is shown by a dashed black line.

SI Figure 2. The speciation of H_2O changes from dominantly hydroxyl (OH^-) in the shallowly sloped portion of the profile to largely H_2O_{mol} in the steep uptick near the rim. The same behavior occurs along transects at cracks (red dashed line), which indicates the steep concentration gradient is an artifact of low temperature hydration unrelated to primary spherulite growth.

SI Figure 3. Water and trace element concentrations in the vicinity of a crack in matrix glass far from spherulite-matrix boundary. Position of crack is shown by large gray line. Water concentration is modified by secondary hydration, but trace elements are not. In decreasing

abundances elements are Mn (white), Rb (pink), Mg (red), Li (orange), Pb (yellow), Ba (green), B (light blue), Cs (medium blue), Sc (dark blue), and Sr (purple). Error bars are shown by black bars unless smaller than symbol size.

SI Figure 4. Results from enthalpy relaxation geospeedometry (a) Smoothed heat capacity (C_p) curves obtained from differential scanning calorimetry of obsidian sample Yell-24. The C_p curve with the high overshoot is the natural curve produced by the first reheating of the sample at 25 K min^{-1}. The previous cooling rate is thus unknown. The following cooling/heating treatments were performed with 25, 20, 15 and 10 K min^{-1}. Stars mark the peak glass transition temperatures (T_g peak) for each C_p curve. The arrow shows the decrease in T_g peak with cooling/heating rate. (b) Best fit to the normalized natural C_p curve. The natural cooling rate estimate is $10^{-5.3}$ °C s^{-1}.

SI Figure 5. Relationships between enrichment (ε), propagation distance (P_Δ), and spherulite size for Rb are shown in A and C. Results for H_2O are shown in B and D. Data are shown as white circles; black lines represent error bars unless smaller than symbol size. The range of ε and P_Δ of profiles around spherulites follow trends with positive slopes.

SI Figure 6. A: Data from spherulite Y24-13. The curve shows the best-fit profile for a medium-sized spherulite. The gray boxes show the range of enrichment at the boundary and concentration at the *e*-fold distance that are ``acceptable''. B-D: Histograms showing the range of parameters

representing, respectively, the nucleation temperature, growth rate, and cooling rate for which an acceptable fit was achieved.

SI Figure 7. Data from a small, medium, and large spherulite (A-C). The curves show the best-fit profiles for all three spherulites simultaneously. The gray boxes show the range of enrichment at the boundary and concentration at the *e*-fold distance that are ``acceptable". D-H: Histograms showing the range of parameters representing the growth rate, cooling rate and nucleation temperature for each spherulite for which an acceptable fit was achieved.

Fig. 1

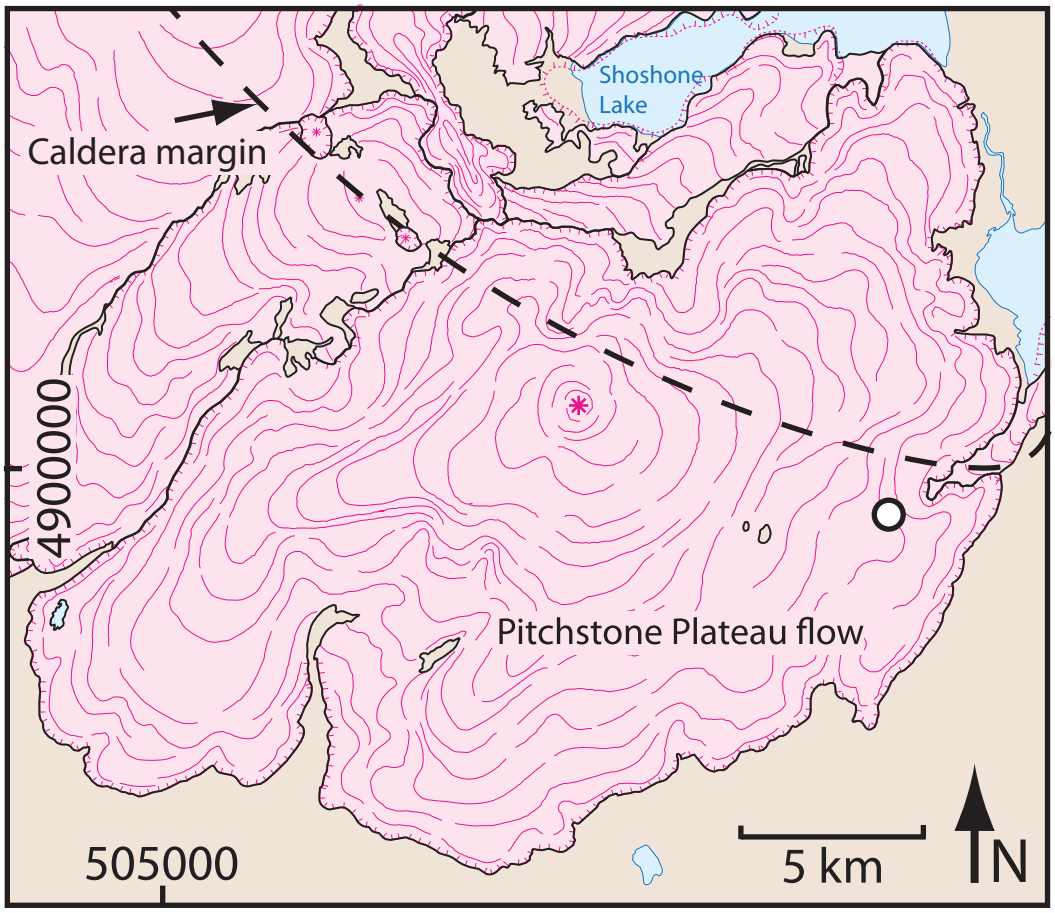
Shoshone
Lake
Caldera margin
4900000
Pitchstone Plateau flow
505000
5 km
N

Fig. 2

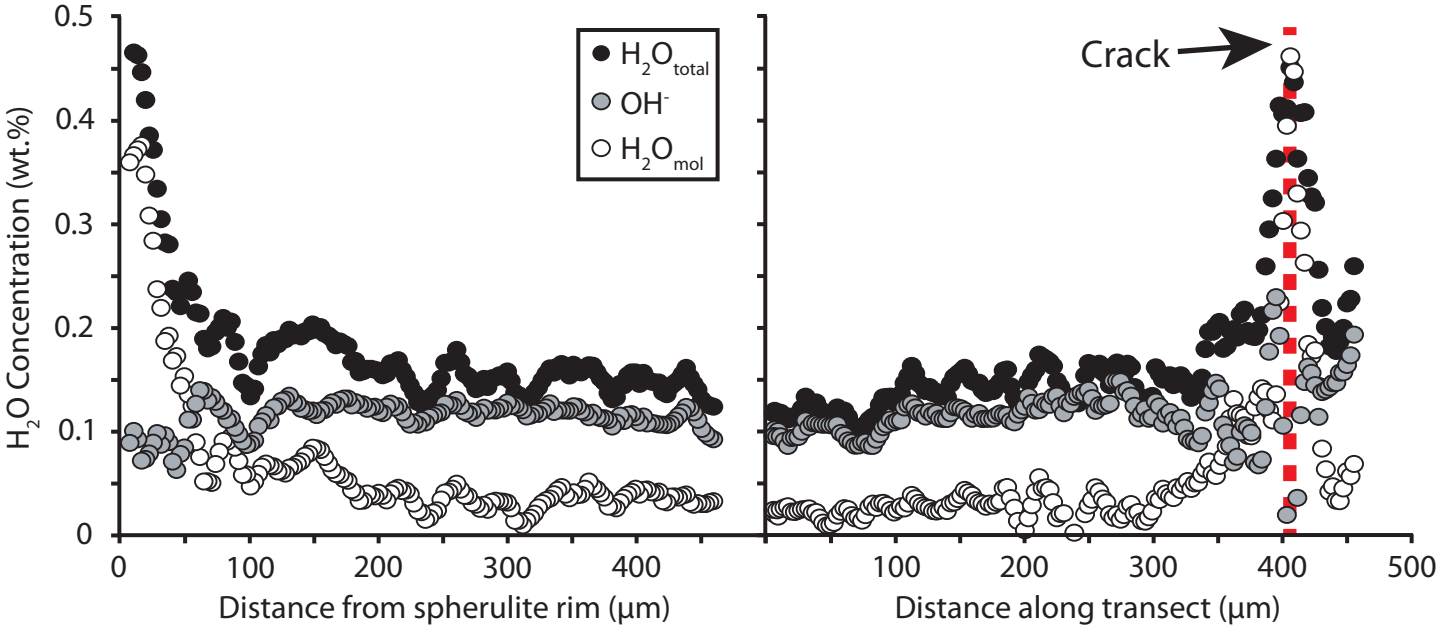
0.5
0.4
0.3
0.2
0.1
0
H2O Concentration (wt.%)
H2Ototal
OH-
H2Omol
Crack
0
100
200
300
400
Distance from spherulite rim (μm)
100
200
300
400
500
Distance along transect (μm)

Fig. 3

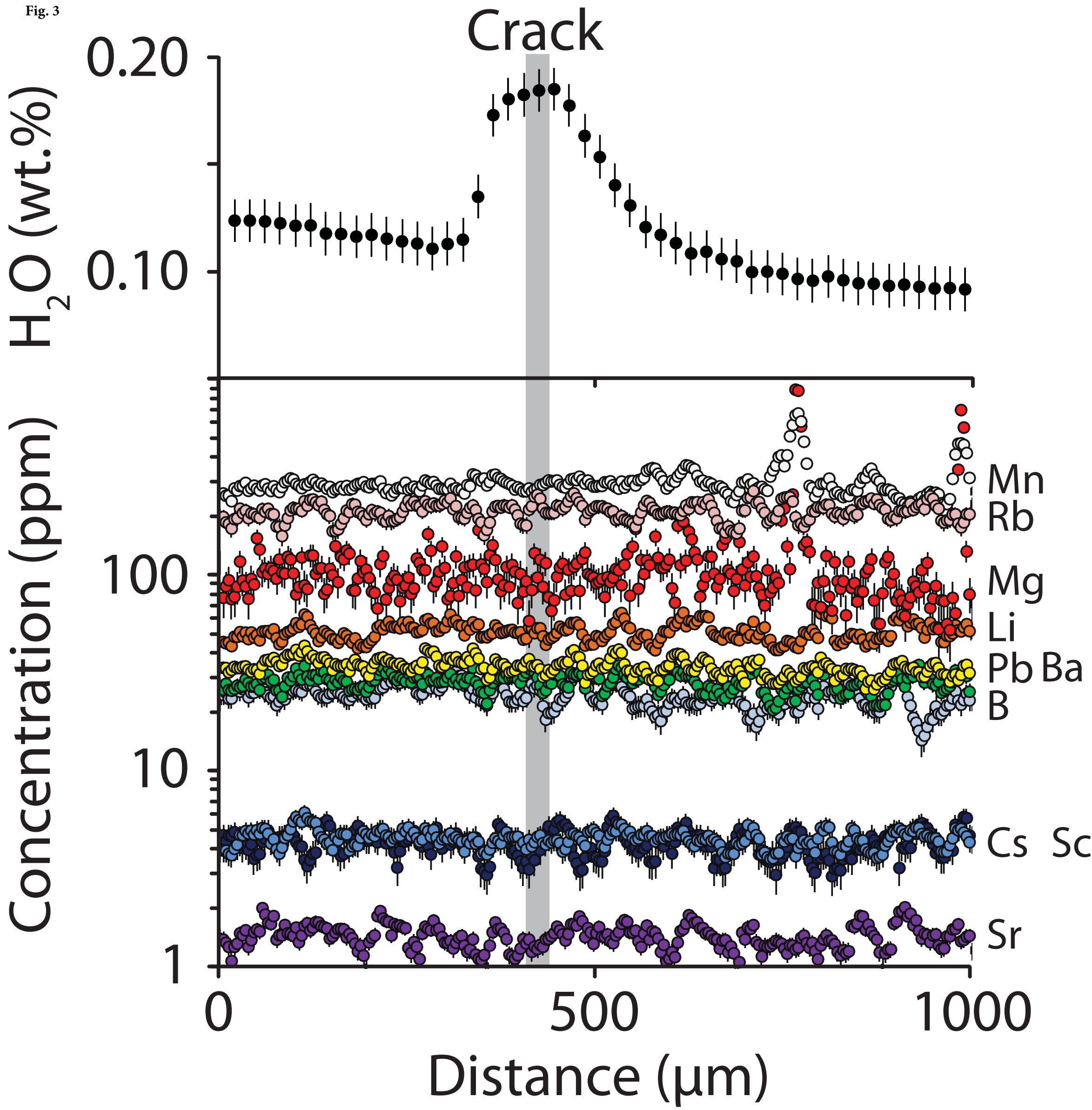
Crack
0.20
0.10
H2O (wt.%)
100
10
1
Concentration (ppm)
Mn
Rb
Mg
Li
Pb
Ba
B
Cs
Sc
Sr
0
500
1000
Distance (μm)

Fig. 4

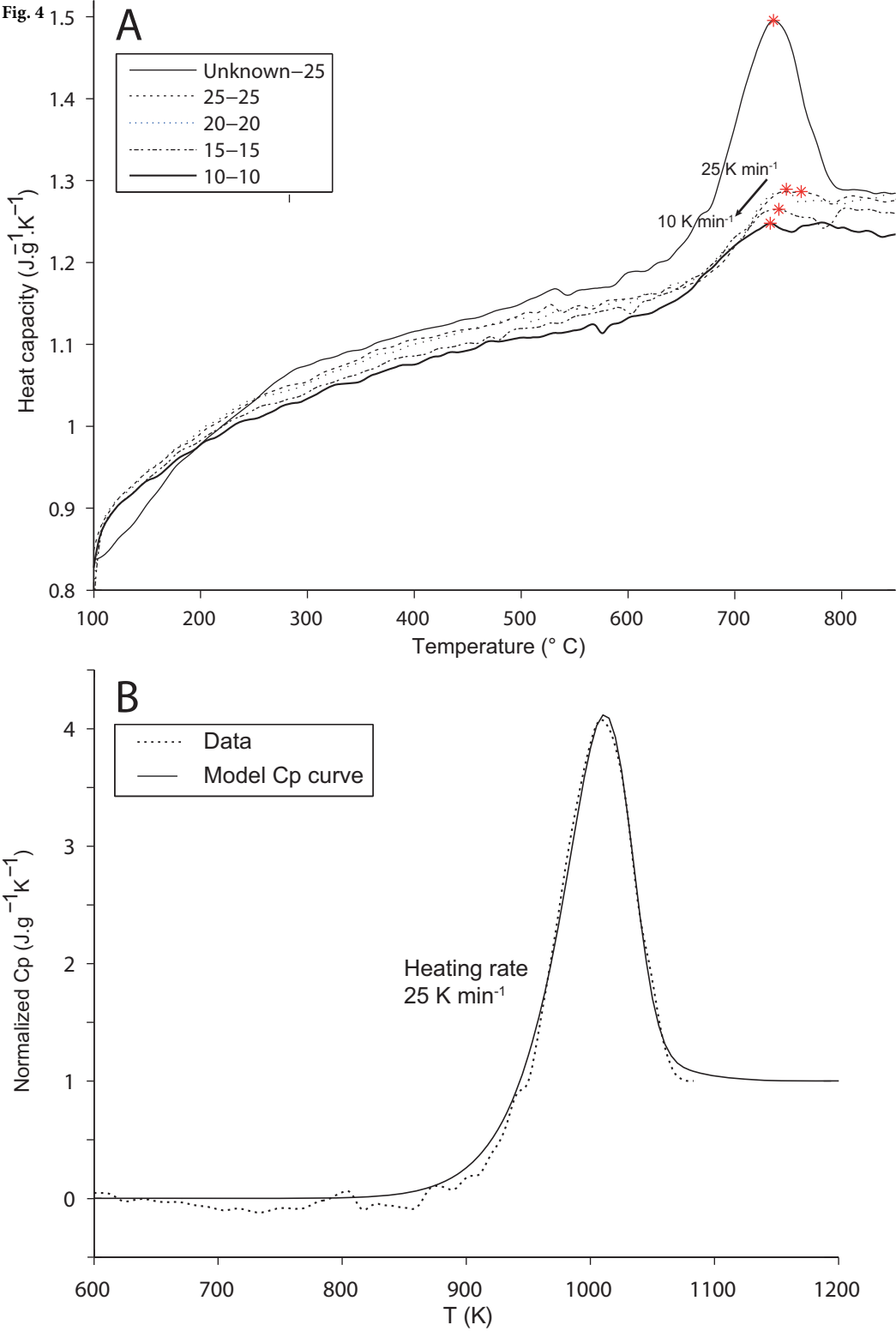
A
Unknown–25
25–25
20–20
15–15
10–10
25 K min-1
10 K min-1
Heat capacity (J.g-1.K-1)
Temperature (° C)
B
Data
Model Cp curve
Heating rate
25 K min-1
Normalized Cp (J.g-1K-1)
T (K)

Fig. 5

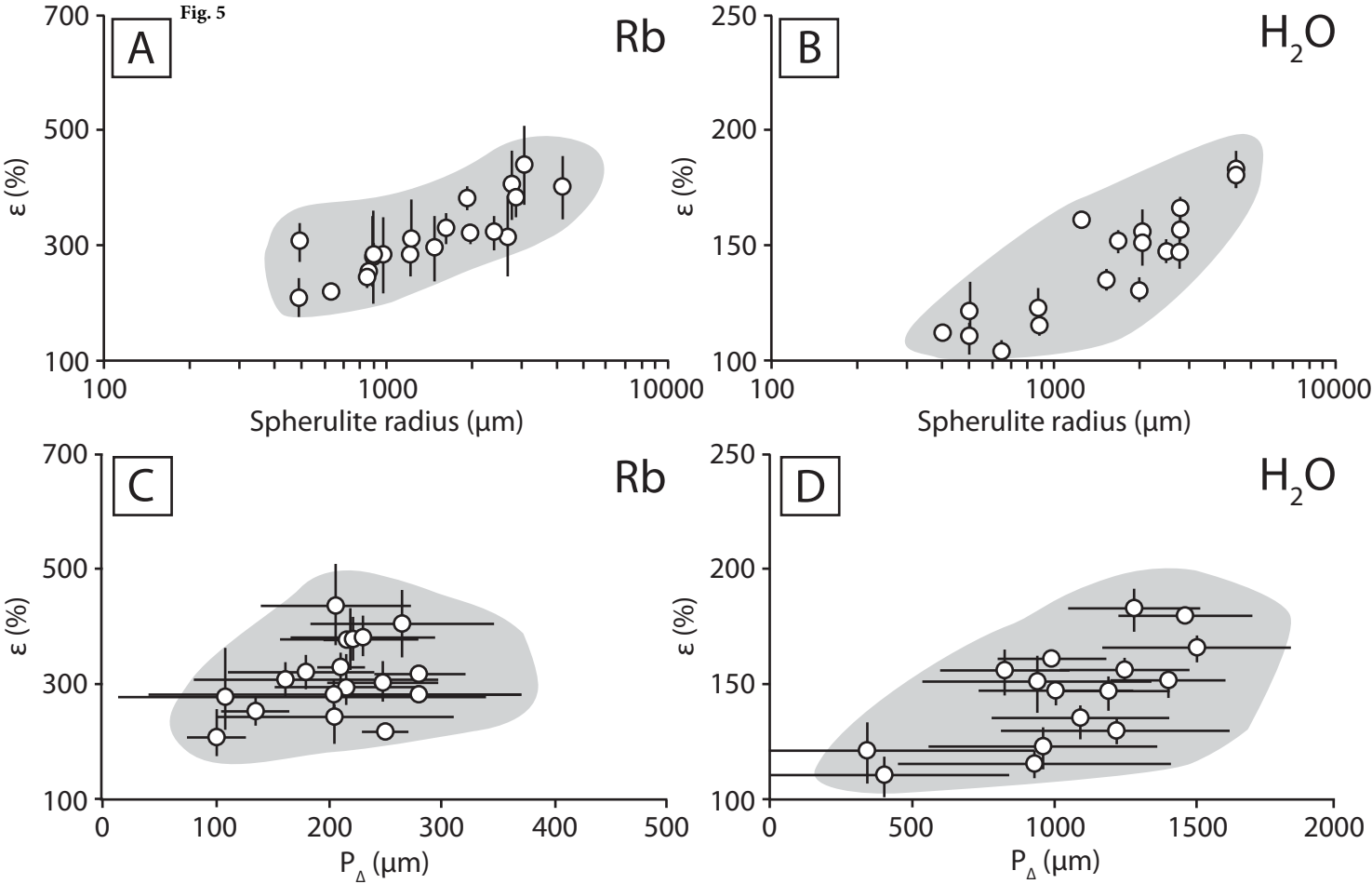
A
Rb
ε (%)
700
500
300
100
100
1000
10000
Spherulite radius (μm)
B
H2O
ε (%)
250
200
150
100
100
1000
10000
Spherulite radius (μm)
C
Rb
ε (%)
700
500
300
100
0
100
200
300
400
500
PΔ (μm)
D
H2O
ε (%)
250
200
150
100
0
500
1000
1500
2000
PΔ (μm)

Fig. 6

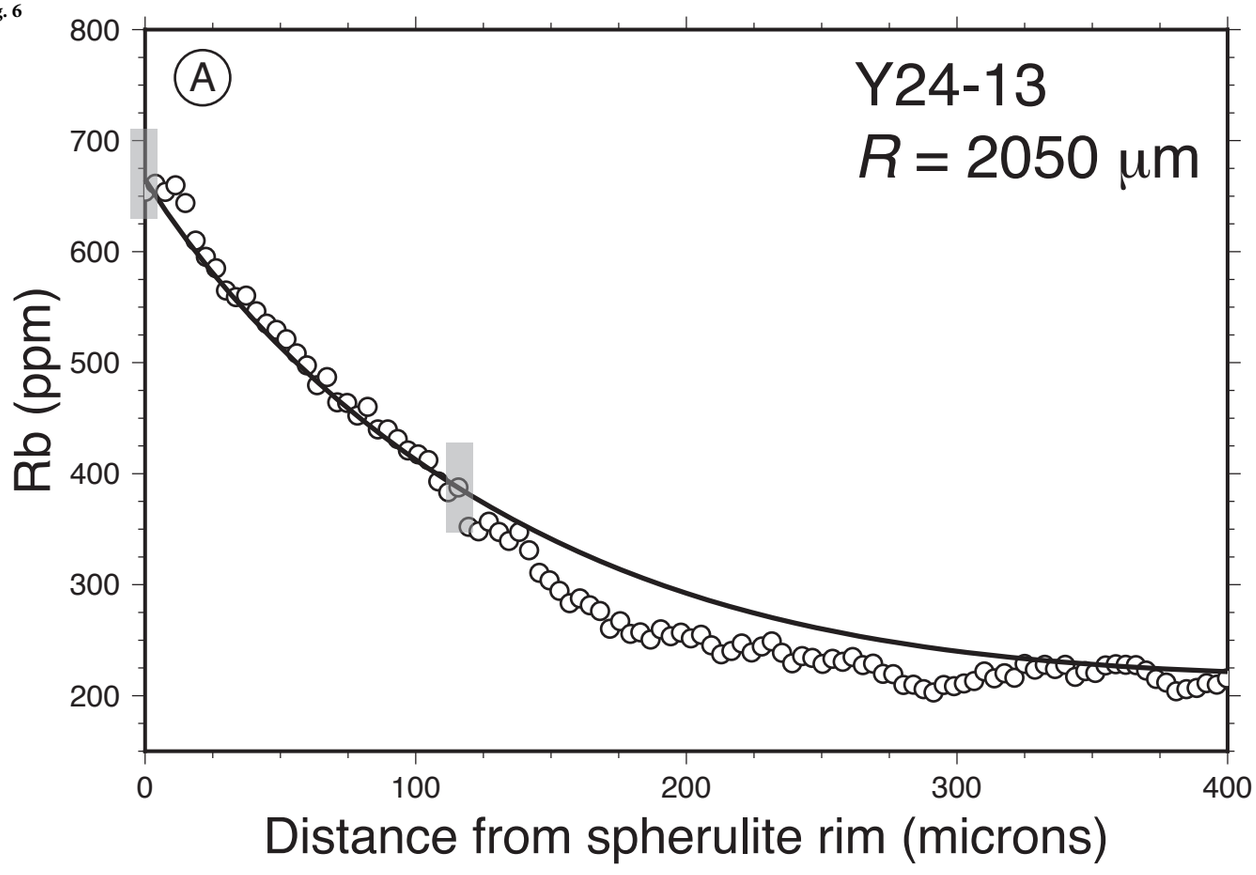
A
Y24-13
R = 2050 μm
Rb (ppm)
Distance from spherulite rim (microns)

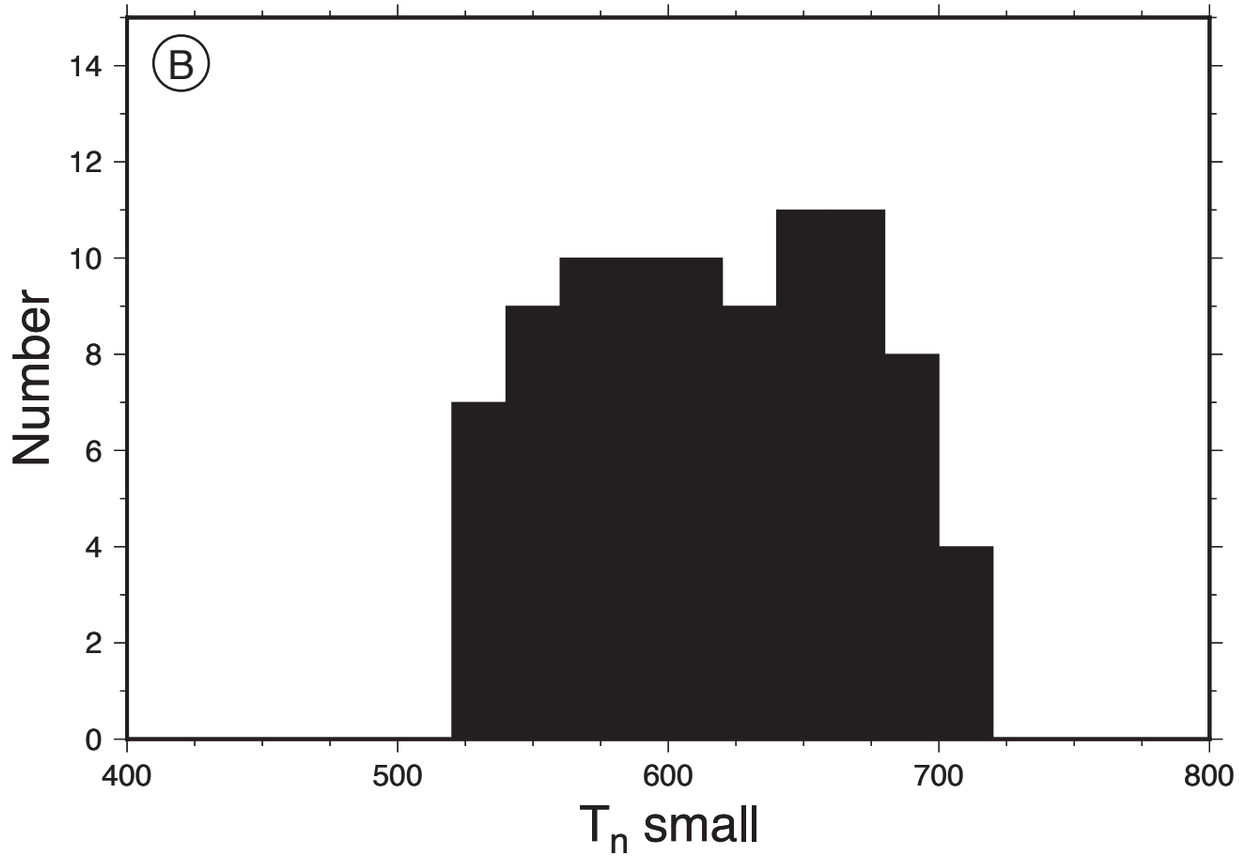
B
Number
T_n small

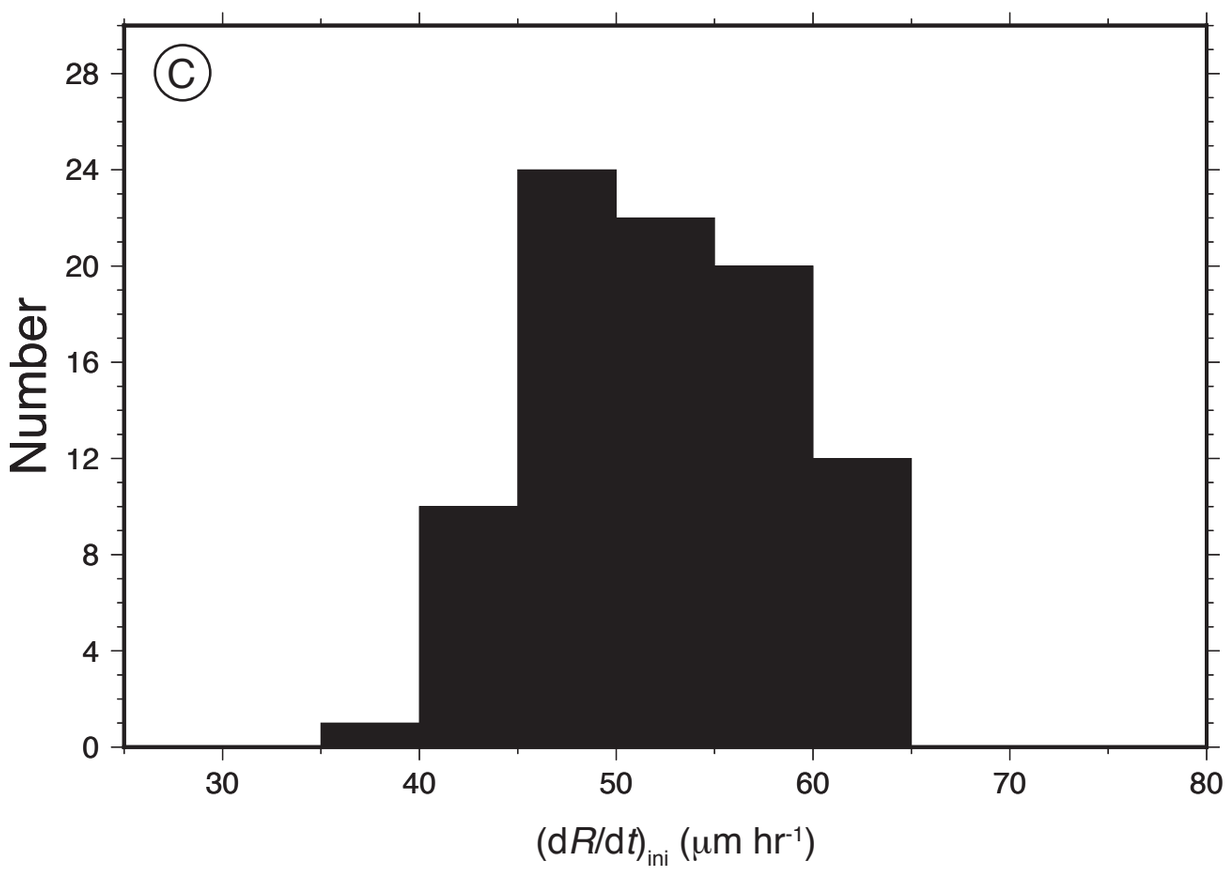
C
Number
(dR/dt)ini (μm hr-1)

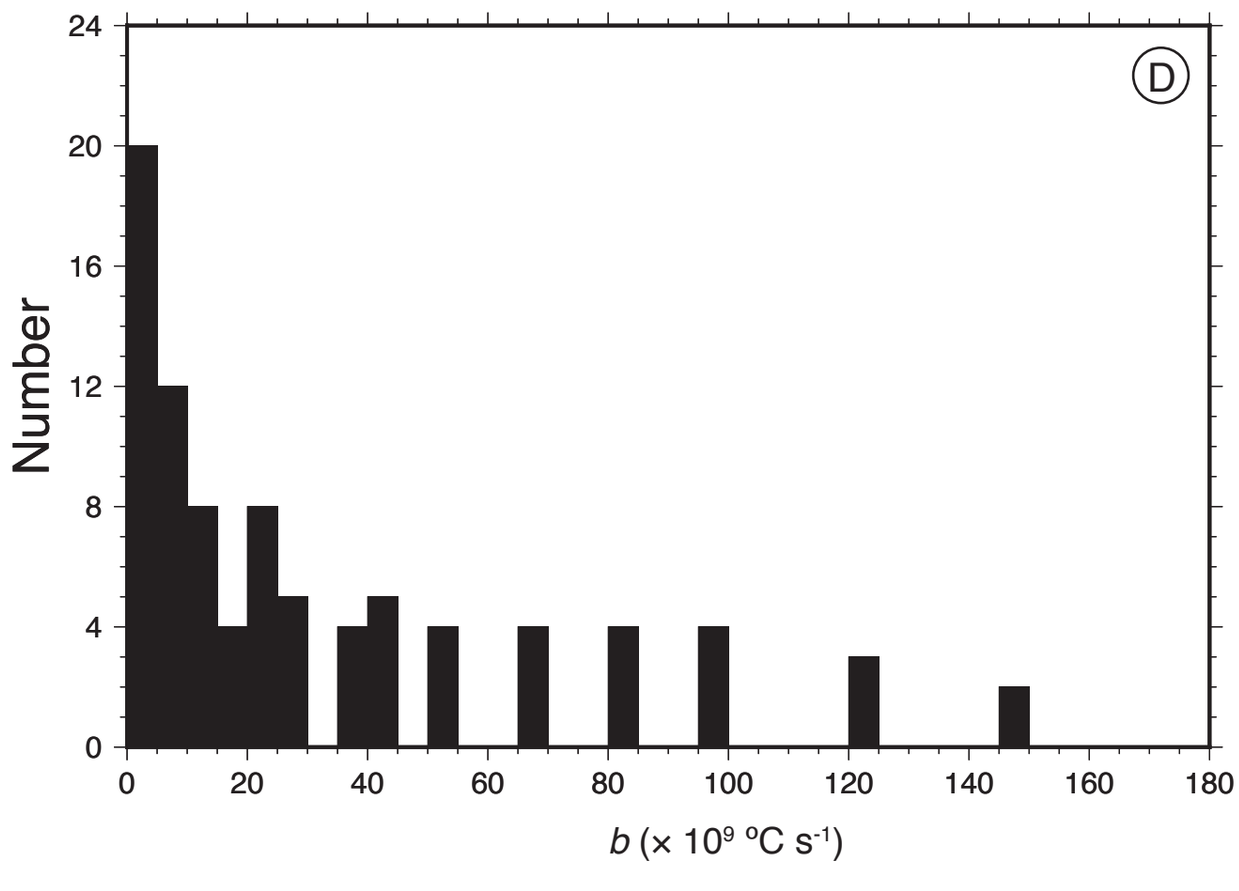
D
Number
b (× 10^9 ºC s-1)

Fig. 7

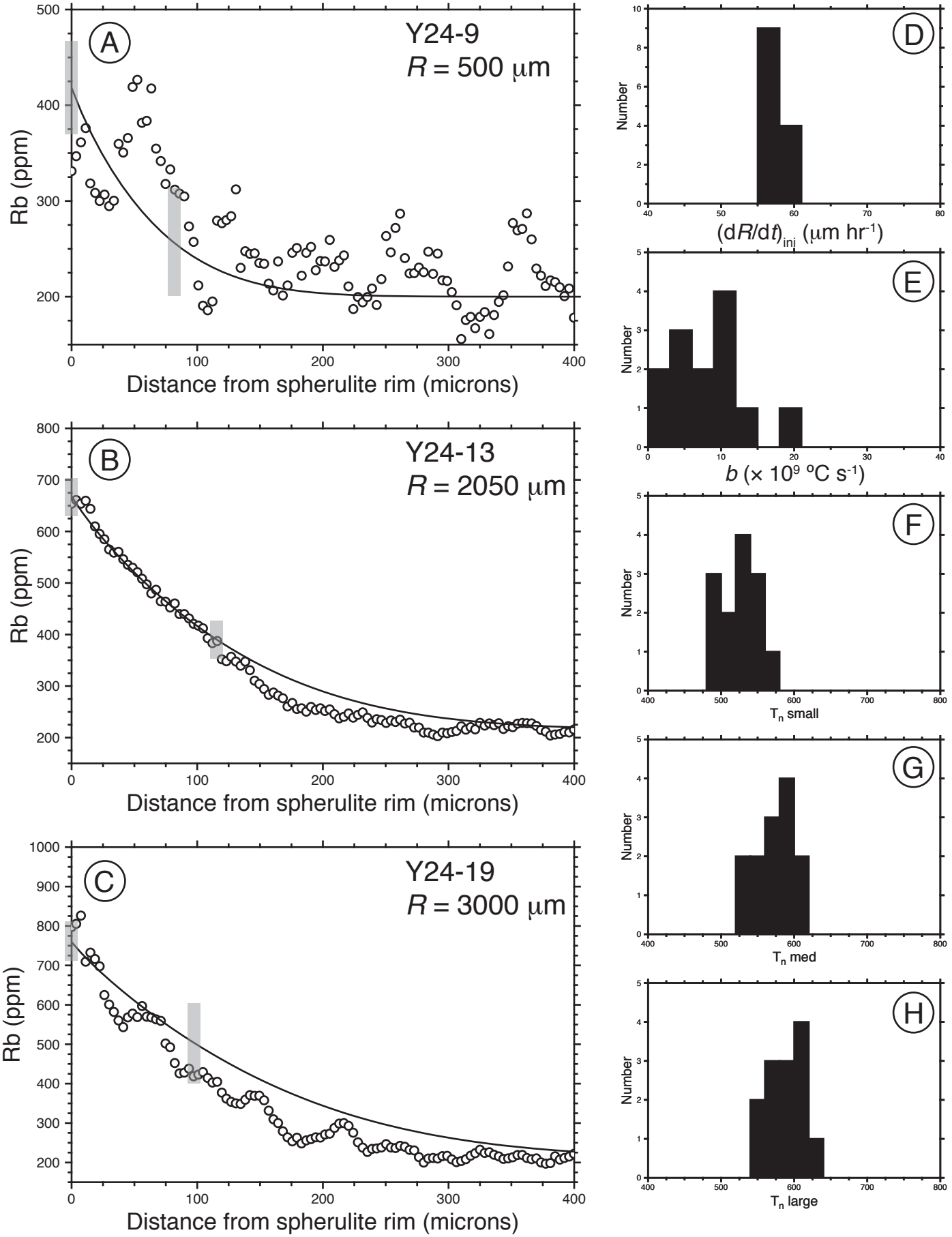
A
Y24-9
R = 500 μm
Rb (ppm)
Distance from spherulite rim (microns)
B
Y24-13
R = 2050 μm
Rb (ppm)
Distance from spherulite rim (microns)
C
Y24-19
R = 3000 μm
Rb (ppm)
Distance from spherulite rim (microns)
D
Number
(dR/dt)ini (μm hr-1)
E
Number
b (× 10^9 °C s-1)
F
Number
Tn small
G
Number
Tn med
H
Number
Tn large

REFERENCES CITED

Christiansen R.L., 2001, The Quaternary and Pliocene Yellowstone Plateau volcanic field of Wyoming, Idaho, and Montana. USGS Professional Paper 729-G, 120 p.

Christiansen, R.L., Lowenstern, J.B., Smith, R.B., Heasler, H., Morgan, L.A., Nathenson, M., and Mastin, L.G., Muffler, L.J.P., Robinson, J.E., 2007, Preliminary assessment of volcanic and hydrothermal hazards in Yellowstone National Park and vicinity: USGS Open-file report 2007–1071, 98 p.

Debolt, M.A., Easteal, A.J., Macedo, P.B., Moynihan, C.T., 1976, Analysis of Structural Relaxation in Glass Using Rate Heating Data: Journal American Ceramic Society, v. 59, p. 16–21, doi: 10.1111/j.1151-2916.1976.tb09377.

Dingwell, D.B., 1998, The glass transition in hydrous granitic melts: Physics of the Earth and Planetary Interiors, v. 107, no. 1–3, p. 1–8, doi: 10.1016/S0031-9201(97)00119-2.

Fenn, P.M., 1977, The nucleation and growth of alkali feldspars from hydrous melts: Canadian Mineralogist v. 15, p. 135-161.

Gardner, J.E., Befus, K.S., Watkins, J., Hesse, M., and Miller, N., 2012, Compositional gradients surrounding spherulites in obsidian and their relationship to spherulite growth and lava cooling: Bulletin of Volcanology, v. 74, no. 8, p. 1865–1879, doi: 10.1007/s00445-012-0642-9.

Giordano, D., Russell, J.K., and Dingwell, D.B., 2008, Viscosity of magmatic liquids: A model: Earth and Planetary Science Letters, v. 271, no. 1–4, p. 123–134, doi: 10.1016/j.epsl.2008.03.038.

Hess, K.-U., Dingwell, D.B., 1996 Viscosities of hydrous leucogranitic melts: A non-Arrhenian model: American Mineralogist, v. 81, p. 1297-1300.

Keith, H.D., and Padden, F.J., 1963, A Phenomenological Theory of Spherulitic Crystallization: Journal of Applied Physics, v. 34, no. 8, p. 2409–2421, doi: 10.1063/1.1702757.

Keith, H.D., and Padden, F.J., 1964, Spherulitic Crystallization from the Melt. I. Fractionation and Impurity Segregation and Their Influence on Crystalline Morphology: Journal of Applied Physics, v. 35, no. 4, p. 1270–1285, doi: 10.1063/1.1713606.

LeVeque, R.J., 2002, Finite volume methods for hyperbolic conservation laws. Cambridge University Press, Cambridge, 558 p.

Lofgren, G., 1971a, Experimentally Produced Devitrification Textures in Natural Rhyolitic Glass: Geological Society of America Bulletin, v. 82, no. 1, p. 111–124, doi: 10.1130/0016-7606(1971)82[111:EPDTIN]2.0.CO;2.

Lofgren, G., 1971b, Spherulitic textures in glassy and crystalline rocks: Journal of Geophysical Research, v. 76, no. 23, p. 5635–5648, doi: 10.1029/JB076i023p05635.

Moynihan, C.T., Easteal, A.J., De BOLT, M.A., Tucker, J., 1976, Dependence of the Fictive Temperature of Glass on Cooling Rate. Journal American Ceramic Society, v. 59, p. 12–16, doi: 10.1111/j.1151-2916.1976.tb09376.

Narayanaswamy, O.S., 1971, A Model of Structural Relaxation in Glass: Journal American Ceramic Society, v. 54, p. 491–498, doi: 10.1111/j.1151-2916.1971.tb12186.

Newman, S., Stolper, E.M., and Epstein, S., 1986, Measurement of water in rhyolitic glasses; calibration of an infrared spectroscopic technique: American Mineralogist, v. 71, no. 11-12, p. 1527–1541.

Ni, H., and Zhang, Y., 2008, H_2O diffusion models in rhyolitic melt with new high pressure data: Chemical Geology, v. 250, no. 1–4, p. 68–78, doi: 10.1016/j.chemgeo.2008.02.011.

Smith, R.K., Tremallo, R.L., and Lofgren, G.E., 2001, Growth of megaspherulites in a rhyolitic vitrophyre: American Mineralogist, v. 86, p. 589-600.

Swanson, S.E., 1977, Relation of nucleation and crystal-growth rate to the development of granitic textures: American Mineralogist, v. 62, p. 966-978.

Watkins, J., Manga, M., Huber, C., and Martin, M., 2009, Diffusion-controlled spherulite growth in obsidian inferred from H2O concentration profiles: Contributions to Mineralogy and Petrology, v. 157, no. 2, p. 163–172.

Zhang, Y., Belcher, R., Ihinger, P.D., Wang, L., Xu, Z., and Newman, S., 1997, New calibration of infrared measurement of dissolved water in rhyolitic glasses: Geochimica et Cosmochimica Acta, v. 61, no. 15, p. 3089–3100, doi: 10.1016/S0016-7037(97)00151-8.

Zhang, Y., Ni, H., and Chen, Y., 2010, Diffusion Data in Silicate Melts: Reviews in Mineralogy and Geochemistry, v. 72, no. 1, p. 311–408, doi: 10.2138/rmg.2010.72.8.